



Dynamic characterization of Ti-4Al-1.5Mn titanium alloy and a simplified approach for shot peening simulation

Nan Su¹ · Minghe Chen¹ · Lansheng Xie¹ · Wenxiang Shi¹ · Feng Luo¹

Received: 8 July 2020 / Accepted: 19 October 2020 / Published online: 2 November 2020
© Springer-Verlag London Ltd., part of Springer Nature 2020

Abstract

To predict the residual stress distribution of the Ti-4Al-1.5Mn (TC2) alloy in the manufacturing process, quickly and accurately, a precise dynamic constitutive model for rheological behavior and a new simplified approach for numerical simulation were proposed. The dynamic stress-strain curves indicate that the enhancement effect and plasticizing of the TC2 alloy are sensitive to high strain rates. The dispersed β particles play an important role in the formation of the adiabatic shear band and not widened significantly. The average relative error of 1.04% and the correlation coefficient of 0.9949 indicate that the modified Johnson-Cook constitutive model well describes the rheological behavior. Then, with the help of the Almen test, an efficient but simplified approach was proposed to achieving coverage and uniform loading in simulation. At last, the residual stress contribution of the TC2 alloy in the shot peening test is in a good agreement with the simulation results by random multipellet model.

Keywords Shot peening · TC2 alloy · Numerical simulation · Residual stress · Dynamic characterization

1 Introduction

Ti-4Al-1.5Mn (subsequently referred to as TC2) is a kind of $\alpha + \beta$ type titanium alloy, which has the characteristics of low density, high specific strength, good plasticity, and weldability [1–3]. Therefore, its sections, sheets, and pipes are widely used in aircraft wings, flaps, tubing, and other components. In order to increase the service life of parts, shot peening is a common process used to improve the fatigue resistance, which can form residual compressive stress inside

the required locations of the components [4–7]. In the actual application, it is an important task to determine the process parameters quickly and accurately with numerical simulation [8–10]. For the TC2 alloy, a precise dynamic constitutive model for rheological behavior and an approach for numerical simulation are very timely studies in shot peening process researches.

The dynamic response of metals at high strain rates is quite different to that of quasi-static deformation. Working in the dynamic response of metals started primarily a few decades ago, and the investigations of various metals at strain rates ranging from 10^{-3} to 10^4 s⁻¹ had been done recently. Via the dynamic experiments on titanium alloy TC4 (Ti-6Al-4V), aluminum alloy AA7075, and magnesium alloy AZ80, Elmagd and Abouridouane found that the flow stress of these materials increased with the strain rate and shown different degrees of strain rate sensitivity [11]. Many scholars had paid attention to the dynamic flow behaviors of titanium alloy and its constitutive model at high strain rate deformation [12–16]. The strain rate sensitivity in the rheological behavior and the adiabatic shear in the microstructure were discussed in these studies. It is found that the hardening effect in high strain rate caused by the kink deformation of the microstructure and the instantaneous deformation concentrates in the narrow area, and then forms an adiabatic shear band (ASB), which occurs in the stress drop stage because of the thermal softening [17].

✉ Minghe Chen
meemhchen@nuaa.edu.cn

Nan Su
mee.sunan@nuaa.edu.cn

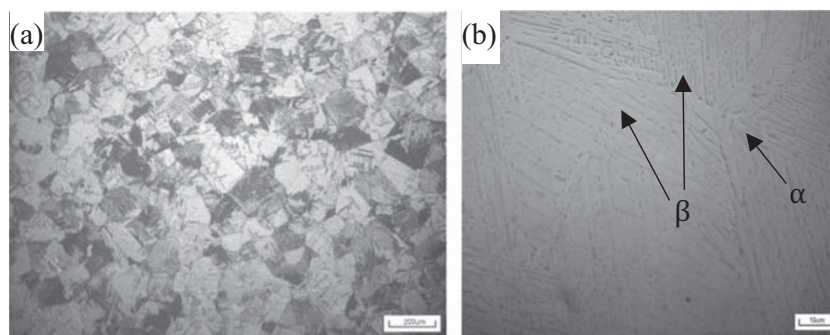
Lansheng Xie
meelsxie@nuaa.edu.cn

Wenxiang Shi
1696439923@qq.com

Feng Luo
1428173207@qq.com

¹ National Key Laboratory of Science and Technology on Helicopter Transmission, Nanjing University of Aeronautics and Astronautics, 210016 Nanjing, People's Republic of China

Fig. 1 Optical micrograph of the original microstructure of the TC2 alloy (a, 50 \times ; b, 1000 \times)



In room temperature, it is a usual method to describe the rheological behavior of materials at high strain rates with Steinberg-Cochran-Guinan (SCG) model [18], Zerilli-Armstrong (Z-A) model [19] and Johnson-Cook (J-C) model [20]. SCG model and Z-A model were constructed based on the principles of material physics; therefore, the number of parameters and complexity of the formulas exceeds the J-C model. For the TC4 alloy, an $\alpha + \beta$ type titanium alloy like TC2, Bhalerao et al. [21] and Che et al. [22] studied the J-C model and modified it to well validate the flow stress prediction, but the prediction of stress response at room temperature is not satisfactory. In summary, the role of diffusion β in the dynamic mechanical characteristics of titanium alloys is rarely studied, and the above-mentioned J-C models cannot be used for the TC2 directly.

Due to its timesaving property that reduces economic cost, the numerical methodology was widely used to acquire further knowledge of shot peening and applied in process optimization [23, 24]. In shot peening simulation, dynamic explicit procedures are better suitable for fast non-linear contact with higher efficiency and robustness [25, 26]. Chen et al. provided a comprehensive review of numerical simulation and optimization of the shot peening found in the existing literature over the past decade [27]. Besides the constitutive model of the target material, coverage and intensity are two important parameters characterizing reproducibility (including quality and effectiveness) in a shot peening process and must be controlled reasonably [28–32]. Building a random multipellet model is a major way to achieve coverage [33, 34]. The random multipellet model setup by Miao et al. and Gangaraj et al.

[35, 36] are more advantageous than the regularly arranged models in predicting the surface state of the target materials, built by Meguid et al. and Majzoobi et al [37, 38]. For realistic shot peening, Chen et al. established a model with 1500 pellets randomly distributed, while the huge amount of calculation brings inefficiency [39]. Meanwhile, numerical results obtained through the area-averaged method were reported to have a better correlation with experimental data measured through the X-ray diffraction method [29, 40, 41].

The purposes of this work are to obtain insights as follows: (a) studying the dynamic mechanical properties of TC2 alloy from 1000 to 5000 s^{-1} at room temperature with Split Hopkinson Pressure Bar (SHPB) technique; (b) providing a precise dynamic constitutive model with adiabatic temperature rise for shot peening simulation; and (c) formulating a new efficient approach to achieve coverage and uniform loading in simulation and predicting the residual stress distribution in the specimen accurately.

2 Experimental procedure

2.1 Experimental procedure

The material used in this study is a TC2 titanium alloy, with main compositions (wt.%) of 3.92 Al, 1.41 Mn, 0.08 Fe, 0.005 N, 0.002 H, 0.15 O, and Ti balance. Figure 1 shows the original microstructure of the as-received TC2 alloy sheet.

According to ASTM E8, the tensile test of the TC2 alloy at the strain rate of $10^{-3} s^{-1}$ was carried out on the electronic

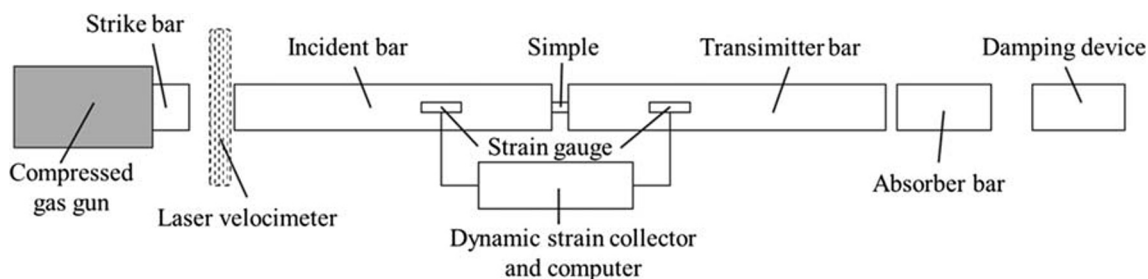


Fig. 2 Schematic of the SHPB system

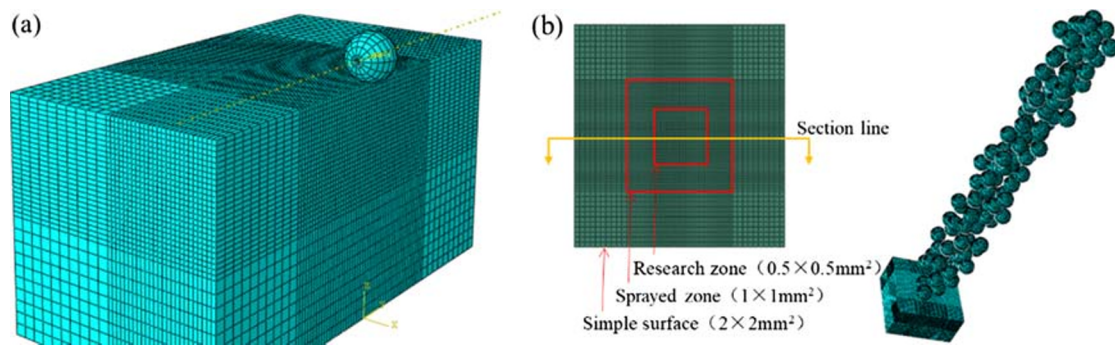


Fig. 3 Illustration of the TC2 alloy model used in the numerical simulation: (a) single pellet and (b) multiple pellets

universal tester UTM-5504X. With a low speed wire-cutting electrical discharge machine and a precision grinder, cylinder specimens for high strain rate dynamic compression test were prepared in the following two sizes: $\varnothing 4\text{mm} \times 2\text{mm}$ and $\varnothing 2\text{mm} \times 2\text{mm}$. Dynamic mechanical behavior of the TC2 alloy at high strain rates that range from 1000 to 5000 s^{-1} was tested using a Split Hopkinson Pressure Bar (SHPB) device and struck three times at each strain rate to ensure the accuracy of the experimental data. The SHPB device consists of a striker bar, an input (or incident) bar, and an output (or transmitted) bar as shown in Fig. 2.

The TC2 alloy specimens after SHPB tests were ground sequentially up to P2000 grit under running water and then

mechanically polished. The treated specimens were etched using 1% HF + 2% HNO_3 + 17% H_2O (volume fraction) solution for 25 s to obtain optical microscopy images by OLYMPUS.

In shot peening experiment study, the TC2 alloy sheet of 3 mm thickness was used as the raw material and cut into $300 \times 600\text{mm}^2$. The shot peening was performed on a CNC shot peening machine MP4000, and the nozzle is 180 mm away from the target along the shot direction perpendicular to the surface. In this shot peening process, at a shot peening flow rate of 8 kg/min, the ceramic pellets AZB425 (diameter 0.425 mm) were driven by an adjustable high-speed air pressure from 0.1 to 0.4 MPa. As calculated in Section 3.3, the shot peening velocity in the tests was set from 30 to 60 m/s.

In order to obtain the residual stress distribution of the shot-peened samples, an LXRC-COMBO type X-ray stress tester was prepared. Before that, portable electrolytic polishing device was used to achieve different depths in the shot-peened area and a new surface of 20 μm deeper was obtained per step. After the test, three random different points at each surface were measured to ensure the reliability, and the average value of these points was calculated as the surface residual stress of each depth.

2.2 Numerical methodology

The numerical analysis elaborated with the FE software ABAQUS and a dynamic explicit calculation mode had been used during the numerical calculation. Within the numerical simulation, the ceramic pellet was considered as a rigid body. To save the calculation time, the 1/2 symmetric model of the cross-section $2 \times 1 \times 1\text{mm}^3$ dimension was constructed in the single pellet simulation. The TC2 alloy has been considered as an elastic-plastic model using C3D8R linear hexahedral elements, constructed and modified in detail in Section 3.2. Refining the mesh in the center to $0.02 \times 0.02 \times 0.02\text{mm}^3$, there are 85,750 finite elements as shown in Fig. 3a. The bottom surface of the substrate has been constrained.

In addition, in order to make the simulation research the same as the actual process, a model of multiple pellets shot

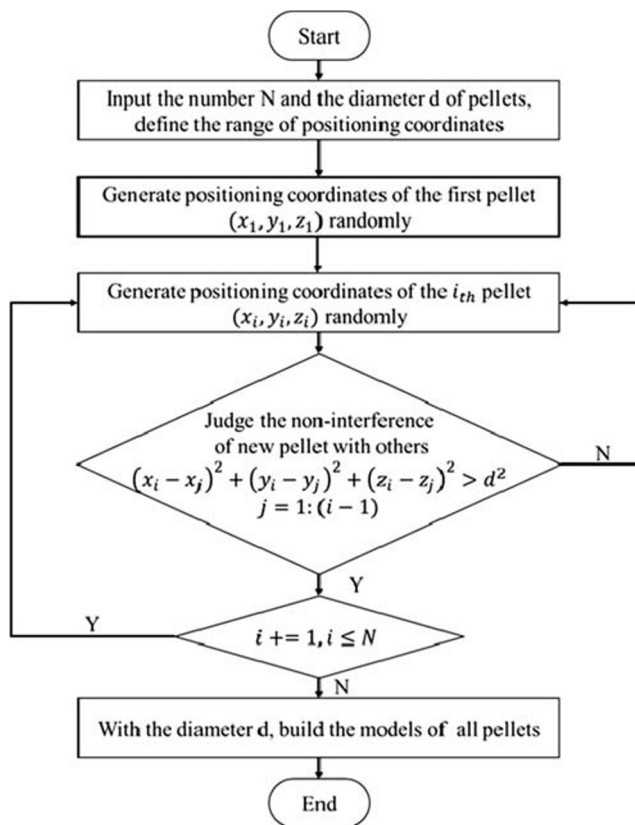


Fig. 4 The algorithm diagram of generating n random pellets

Table 1 The material parameters of SAE 1070 in the Almen test

Basic material parameters			Parameters of Johnson-Cook constitutive model			
Density ($t\text{ mm}^{-3}$)	Young's modulus (MPa)	Poisson ratio	<i>A</i>	<i>B</i>	<i>C</i>	<i>n</i>
7.8E-9	2.05E5	0.29	1408	600.8	0.0134	0.234

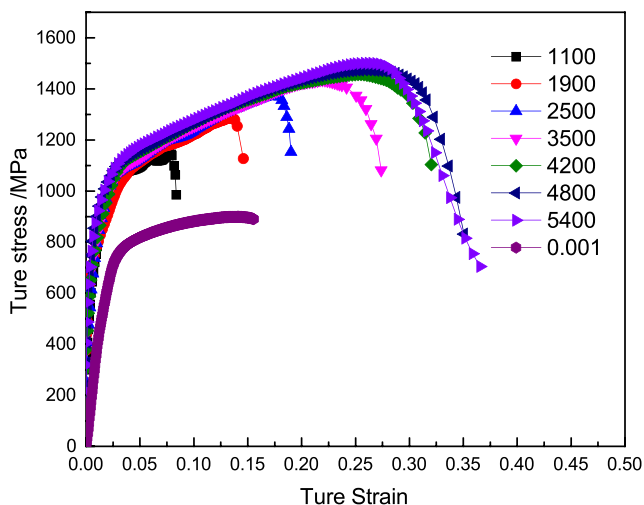
peening was elaborated. As shown in Fig. 3b, it included n random pellets in the rectangular parallelepiped, achieving close to 100% coverage in the $1 \times 1\text{ mm}^2$ area.

In order to simplify the simulation based on the shot peening process, some assumptions were set as follows in this study: each pellet hits the material only once and ignores the collision between the pellets. After defining the center of the sprayed zone as the origin of coordinates, the positioning coordinates of n random pellets should follow Eq. (1).

$$\begin{cases} x_{\min} < x_i < x_{\max} \\ y_{\min} < y_i < y_{\max} \\ z_{\min} < z_i < z_{\max} \end{cases} \quad (1)$$

Where, (x_i, y_i, z_i) is the positioning coordinate of the i_{th} random pellet and x_{\min} , x_{\max} , y_{\min} , and y_{\max} are the boundary of the sprayed area. The value of z_{\min} equals to pellet radius, and it is 0.2125 mm in this case. With the change of z_{\max} , running time and coverage of the process simulation could be controlled properly. With the random function of MATLAB, the positioning coordinates of n random pellets generated follow an algorithm, shown graphically in Fig. 4.

The number of random pellets n determined by the crater diameter, deformed by single-pellet impact on the target surface. Besides the material properties of pellets and as-received TC2 alloy, the most important factor affecting the crater diameter is the shot peening intensity, which can be expressed

**Fig. 5** Stress-strain curve of TC2 alloy under the quasi-static and dynamic conditions

by Almen gage with standards of SAE J422 and AMS 2430 [42]. Table 1 lists the material parameters of specimens used in the Almen test, which is SAE 1070.

Equation (2) provides an expression for the moment of Almen test strip at different conditions, mainly derived from the residual stress distribution. The bending arc height value of Almen gage, that is, shot peening intensity, was caused by different process parameters and described through Eq. (3).

$$M = \int_s \sigma_x(z) z dS \quad (2)$$

$$H = \frac{3ML^2}{2EBh^3} \quad (3)$$

In Eqs. (2) and (3), M is the bending moment, S is the section area, z is the distance from the element to the target surface, and $\sigma_x(z)$ is the average transverse residual stress of the element at a distance z to the surface, that is S_{11} in the analysis result with ABAQUS. H is the value arc height; E is elastic modulus; L is half the distance between the support points of the arc height gauge; and B and h are the width and thickness of the Almen gage.

Finally, with the shot peening intensity determined by Almen test, the loading in the process test and numerical simulation achieved are almost the same. The shot peening process parameters are unified in simulation and production, which include material, processing time (coverage), shot peening direction, and shot intensity. Then, the results of the simulation and tests are compared to evaluate the feasibility and accuracy of the simulation path in this research.

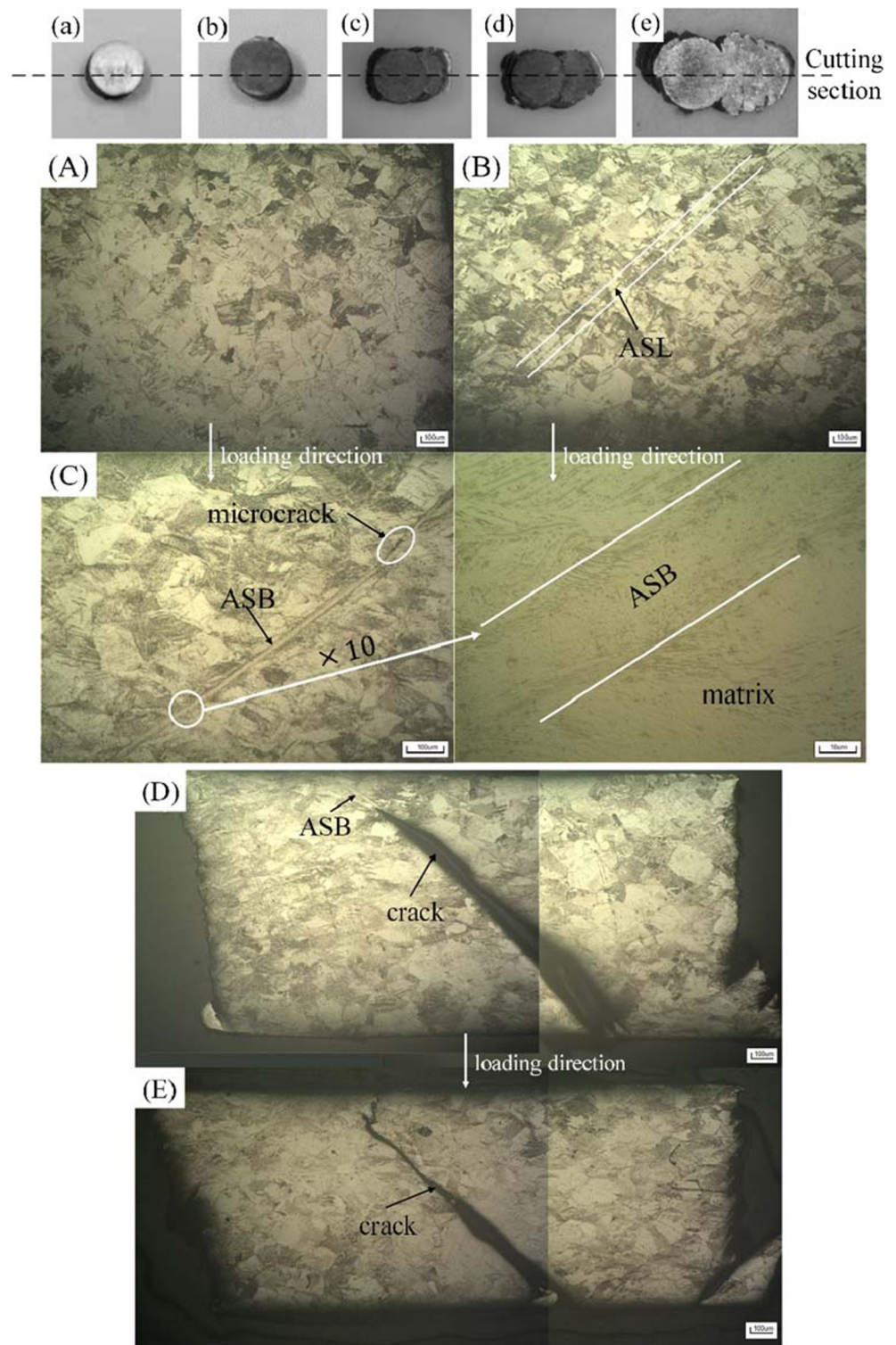
3 Results and discussion

3.1 Dynamic mechanical properties

3.1.1 Stress versus strain response

Details of stress-strain curves of different samples at high strain rates of 1100, 1900, 2500, 3500, 4200, 4800, and 5400 s^{-1} are revealed in Fig. 5. The flow stress of the TC2 alloy at high strain rates is significantly higher than quasi-static conditions, and with the slopes of the steady-state rheological stage at different strain rates, it can be analyzed that the

Fig. 6 Photos and microstructures of the specimens after dynamic compression test: (a, A) 1100 s^{-1} ; (b, B) 2500 s^{-1} ; (c, C) 3500 s^{-1} ; (d, D) 4200 s^{-1} ; (e, E) 4800 s^{-1}



dynamic strain hardening at high strain rate is greater than that of 0.001 s^{-1} .

The dynamic rheological behavior of the TC2 alloy at high strain rates is the result of strain hardening and thermal softening, while the effect of strain hardening weakens by thermal softening. As shown in Fig. 5, because of strain hardening, the

dynamic rheological stress increases faster at the low strain stage. However, the stress growth rate of the TC2 alloy slows down in the high strain stage, and even a slow decline phenomenon occurs at the higher strain rates, which can be explained with the dominance of the thermal softening effect. The instantaneous dynamic plastic deformation of the TC2

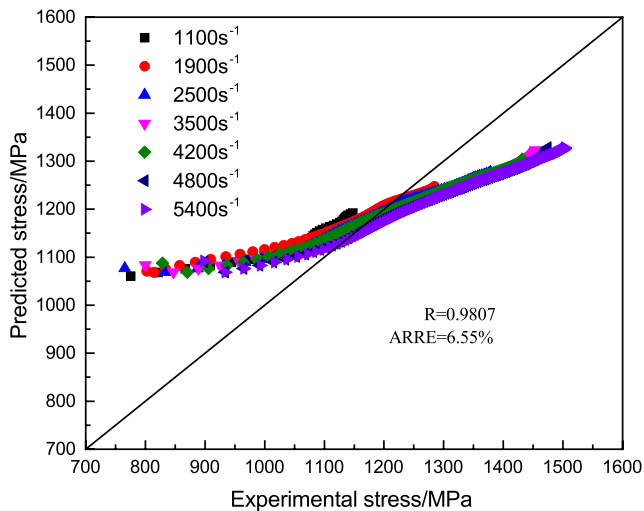


Fig. 7 Accuracy of initial Johnson-Cook model for TC2 alloy at high strain rate

alloy at room temperature is an approximate adiabatic process, and the energy generated by high-speed plastic deformation leads to the thermal softening.

With the comparative analysis of ultimate strain values and maximum stresses at different strain rates in Fig. 5, the dynamic mechanical properties of the TC2 alloy were summed up as follows. First, the flow stress of the TC2 alloy and the maximum stress in a fixed strain rate increase with the strain rate, which indicates the existence of a significant enhancement effect of strain rate. Second, the ultimate strain of the TC2 alloy at each strain rate increases with strain rate and extends the stable plastic deformation stage, which demonstrates a significant strain rate plasticizing effect. However, there is no big change in the ultimate strain value when the

strain rate exceeds 4800 s^{-1} , that is, the plasticizing effect subsides. Meanwhile, the enhancement effect of strain rate is obviously weakening.

3.1.2 Microstructure characterization

In order to analyze the internal mechanism of the dynamic mechanical properties exhibited previously, photos (a–e) and microstructures (A–E) are presented in Fig. 6 except for the samples that are obviously broken into two parts at the strain rate of 5400 s^{-1} . Compared with the as-received material, there is no obvious change in the grain size and shape of the compressed sample at a low dynamic strain rate. However, at a strain rate of 2500 s^{-1} (Fig. 6b), an adiabatic shear line (ASL) about 45° to the loading direction is observed. In addition, there is an obvious 45° adiabatic shear band (ASB) and a certain plastic flow on both sides in the samples at 3500 s^{-1} (Fig. 6c). Beyond the elastic deformation stage, more kinetic energy promotes plastic deformation along the slip surface with more point and surface defects, and the instantaneous deformation is concentrated on the weakest shear surface to form an adiabatic shear band. The temperature caused by high-speed deformation promotes the acceleration of atomic motion, and then the grains are twisted and the shear band is formed. At the same time, some micro-cracks appear in the adiabatic shear zone. With the increasing strain rate (Fig. 6d,e), the adiabatic temperature rise continues to increase, the resistance to dynamic deformation of the TC2 alloy decreases, and the increasing strain promotes the propagation of micro-cracks in the adiabatic shear zone, which eventually results in shear fracture of these samples.

Comparing the width of ASBs at different strain rates, the value does not change significantly with the increasing strain

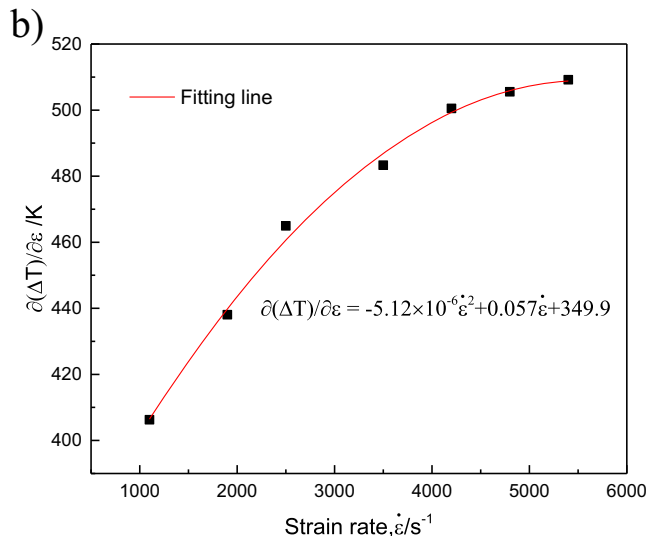
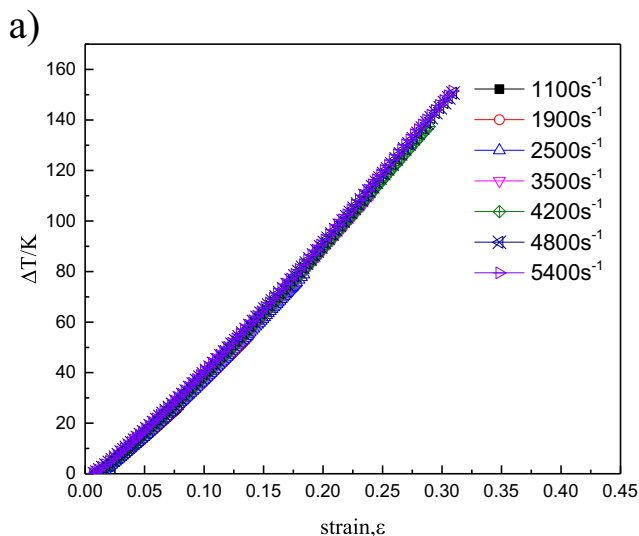


Fig. 8 The relationship of ΔT with ε (a) and $\partial(\Delta T)/\partial \varepsilon$ with $\dot{\varepsilon}$ (b)

rate. The black particles (β phase) gather on the boundary of ASB, which are distributed in the matrix uniformly, while the density in the ASB is decreasing. According to the picture of the partially enlarged microstructure in Fig. 6c, the dispersed β phase in the TC2 alloy slips to the boundary of the ASB because of the dynamic stress, and two obvious blocking bands formed. Meanwhile, the excess impact energy promotes the generation and propagation of micro-cracks at the strain rate of 3500 s^{-1} . The energy provided by the higher strain rates (Fig. 6d,e) cannot move the slip block of β -accumulated further to both sides; instead, it accelerates the sharp deformation of the low-resistance α -phase matrix and the fracture of the sample along the ASBs. Therefore, the width of ASBs has not increased significantly but the samples split in half.

3.2 Johnson-Cook constitutive model and modification

3.2.1 Initial model

The precise dynamic constitutive model directly affects the dynamic mechanical response accuracy of materials in simulation. A material model that accurately describes the dynamic stress-strain relationship is the basis of the shot peening process simulation. The traditional formula of the Johnson-Cook model includes strain hardening term, strain rate term, and temperature term, which respectively describe the effect of strain hardening, strain rate hardening, and thermal softening during plastic deformation, as shown in Eq. (4).

$$\sigma = (A + B\varepsilon^n) \left(1 + C \ln \frac{\dot{\varepsilon}}{\varepsilon_0} \right) (1 - T^{*m}) \tag{4}$$

Where, $T^* = (T - T_r)/(T_m - T_r)$, A, B, C, n are the material correlation coefficients of hardening, determined by experiment. ε_0 is the reference strain rate; m is the sensitivity coefficient of temperature; T is the deformation temperature; T_r is the reference temperature (usually room temperature); and T_m is the melting point of the material. The shot peening process is taken in the room temperature, and the temperature term of the traditional JC model can be regarded as 1. Then, compute the other parameters in two steps. First, taking 0.001 s^{-1} as reference strain rate, the values of A, B, n obtained by the non-linear fit of the strain-stress curve without elastic section, $A = 679.8\text{MPa}$, $B = 458.5\text{MPa}$, $n = 0.324$. Second, the C at each strain rate was calculated from the fitting of the stress-strain curve, and the average of them is 0.0255. In summary, the model can be expressed by Eq. (5).

$$\sigma = (679.8 + 458.5\varepsilon^{0.324}) \left(1 + 0.0255 \ln \frac{\dot{\varepsilon}}{0.001} \right) \tag{5}$$

The average relative error (AARE) and correlation coefficient (R) were used to measure the fitting accuracy of this model, and the details are shown as following formulas.

$$AARE = \frac{1}{N} \sum_{i=1}^N |(E_i - P_i)/E_i| \times 100\% \tag{6}$$

$$R = \frac{\sum_{i=1}^N (E_i - \bar{E})(P_i - \bar{P})}{\sqrt{\sum_{i=1}^N (E_i - \bar{E})^2 (P_i - \bar{P})^2}} \tag{7}$$

With the comparison between the fitted results of initial Johnson-Cook model and experimental data, as shown in

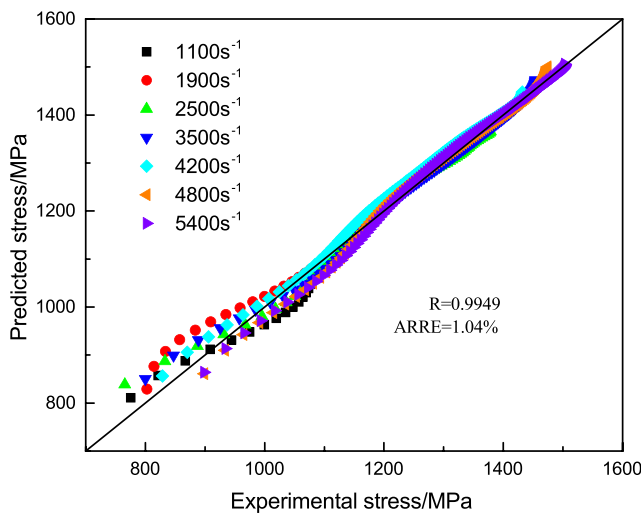


Fig. 9 Accuracy of the modified Johnson-Cook model for TC2 alloy at high strain rate

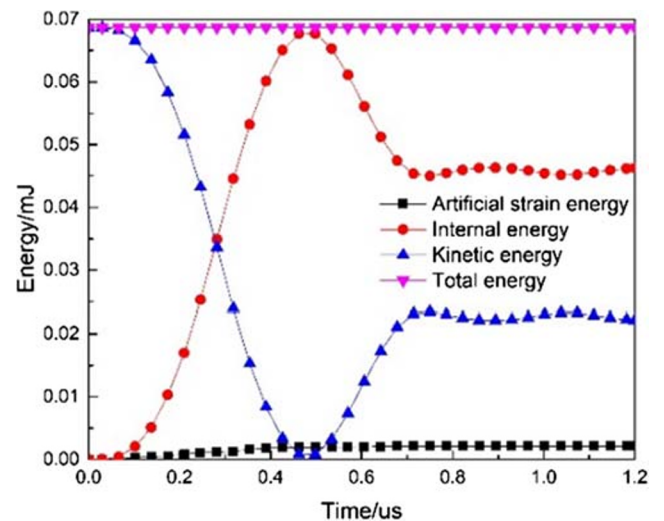


Fig. 10 Energy versus time curve of the model in the single pellet impact

Fig. 7, the AARE = 0.9807 and the R = 6.55%. Obviously, this model has not yet to meet the requirement for guaranteeing simulation accuracy.

3.2.2 Modified model with adiabatic temperature rise

As discussed in the analysis of the thermal softening effect previously, the temperature rise of adiabatic shear affects the rheological behavior of the TC2 alloy at high strain rates. It is important to incorporate adiabatic heating into the model, which is caused by transient plastic strain accumulation. In the room temperature, the effect of thermal softening comes from the comprehensive action of strain and strain rate, which can be defined as Eq. (8). Meanwhile, Eq. (9) has been extensively used to estimate the temperature rise (ΔT) during high strain rate deformation.

$$T_{\Delta} = \left(\frac{\Delta T}{T_m - T_r} \right)^k = f(\varepsilon, \dot{\varepsilon}) \tag{8}$$

$$\Delta T = \frac{\beta}{\rho C_p} \int_0^{\varepsilon_p} \sigma d\varepsilon_p \tag{9}$$

Where, T_{Δ} is the temperature term; k is the corresponding sensitivity coefficient of temperature; ρ is the material density, 4550 kg/m³; C_p is the specific heat capacity of the material, 0.526 kJ/(kg·K); β is the conversion coefficient from deformation work to thermal energy; and the prevalent perspective is to define β as 0.9; and ε_p and σ are the plastic strain and corresponding stress at high strain rates, respectively.

With Eq. (9) and stress-strain curves at different strain rates, the adiabatic temperature rise ΔT can be

calculated, and the relationship between ΔT and the strain ε is shown in Fig. 8. The value of the adiabatic temperature rise increases with the strain and shows an approximately linear relationship.

With the slope $\partial(\Delta T)/\partial\varepsilon$ at each strain rate, scattered points are listed in Fig. 8b. These points show a clear parabolic function relationship, defined as:

$$\partial(\Delta T)/\partial\varepsilon = D \cdot \varepsilon^2 + E \cdot \dot{\varepsilon} + F \tag{10}$$

Calculated by integration, the adiabatic temperature rise can be expressed as in the following formula:

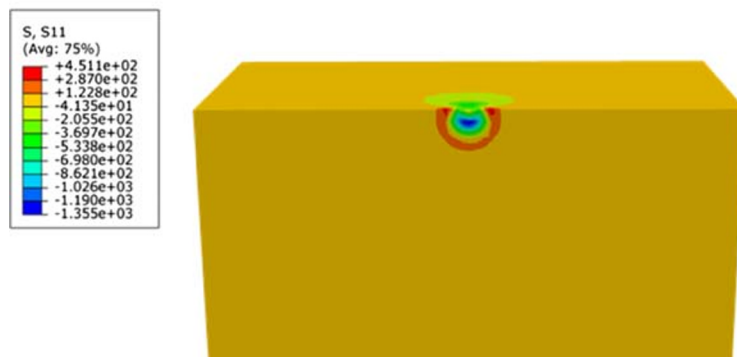
$$\Delta T = \int_0^{\varepsilon_p} (\partial(\Delta T)/\partial\varepsilon) d\varepsilon_p = \left(D \cdot \varepsilon^2 + E \cdot \dot{\varepsilon} + F \right) \cdot \varepsilon_p + G \tag{11}$$

Where, D , E , F , G are the constants; ε_p is the plastic strain; and $\varepsilon_p = \varepsilon - 0.008$. When plastic strain equals 0, the adiabatic temperature rise ΔT is also 0 and substituted into Eq. (11) to get $G = 0$. Other parameters are obtained by binomial fitting in Fig. 8b. The modified Johnson-Cook model has the form of Eq. (12), and all the parameters can be computed by following the fitting procedures described previously.

$$\sigma = (A + B\varepsilon^n) \left(1 + C \ln \frac{\dot{\varepsilon}}{\dot{\varepsilon}_0} \right) \left[\frac{(D \cdot \varepsilon^2 + E \cdot \dot{\varepsilon} + F) \cdot \varepsilon_p}{T_m - T_r} \right]^k \tag{12}$$

In Origin 2015, for the stress-strain curve at each strain rate, the corresponding C and k were obtained

a)



b)

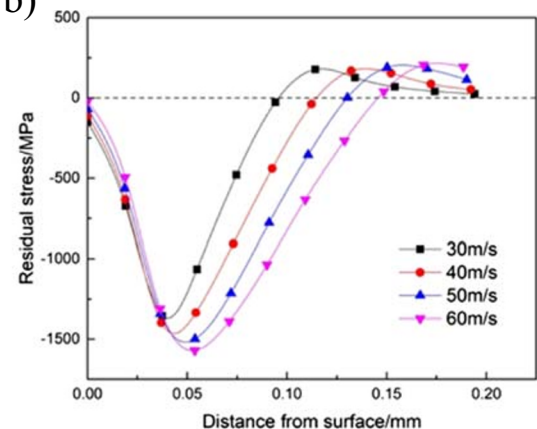


Fig. 11 Residual stress distribution cloud (a) and changes in residual stress along the depth (b)

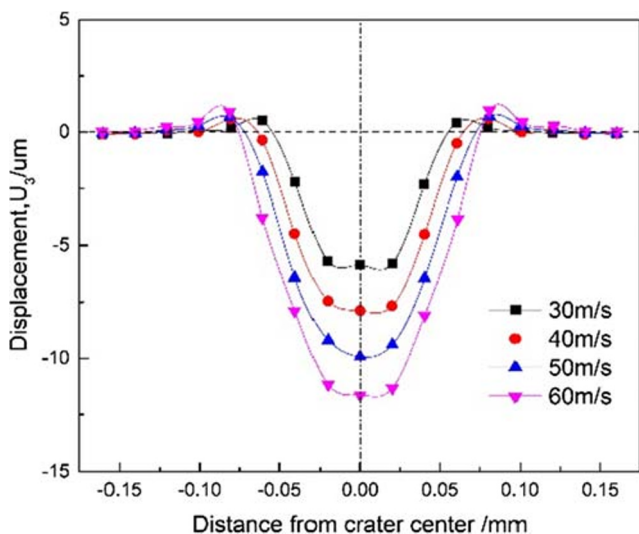


Fig. 12 Displacement curve of the TC2 alloy surface in the crater section

by nonlinear fitting with Eq. (12). Finally, the average values of k and C are 0.089 and 0.062, respectively, and the detail modified Johnson-Cook model is:

$$\sigma = (679.8 + 458.5\varepsilon^{0.324}) \left(1 + 0.054 \ln \frac{\dot{\varepsilon}}{\varepsilon_0} \right) \left[\frac{(-5.12 \times 10^{-6} \cdot \varepsilon^2 + 0.057 \cdot \dot{\varepsilon} + 349.9) \cdot (\varepsilon - 0.008)}{T_m - T_r} \right]^{0.069} \quad (13)$$

As seen in Fig. 9, the scatter of experimental and predicted stresses is very close to the equal line. With a modified Johnson-Cook model, the AARE = 1.04% and the R = 0.9949. That is, a high-precision material model for TC2 alloy shot peening simulation has been obtained.

3.3 Simulation of shot peening process

3.3.1 Single pellet

In order to achieve the uniformity of the shot peening test and simulation process, it is necessary to ensure that the dynamic response of the TC2 alloy and loading in the simulation are the same to the test procedure. The constitutive model keeps the mechanical response accuracy of the TC2 alloy, and loading in simulation depends on the shot speed of pellets except for the shot peening angle 90°. The actual velocity of pellets in shot peening was determined by the projectile diameter, shot gas pressure, and shot peening flow rate. The average velocity of the shot peening was calculated by an empirical formula.

$$v = \frac{163.5p}{1.53m + 10p} + \frac{295p}{0.598d + 10p} + 48.3p \quad (14)$$

Where, v is the average velocity of the shot peening (m/s); d is the projectile diameter (mm); p is shot gas pressure (MPa);

and m is the shot peening flow rate (kg/min). The CNC shot peening machine MP4000 in this research provides a shot peening flow rate of 8 kg/min and an adjustable air pressure from 0.1 to 0.4 MPa. The pellets used in this test were AZB425 with a diameter of 0.425 mm, and the achievable shot peening average velocity range is 30–60 m/s via calculation with Eq. (14). Because the loading is a uniform speed without acceleration, the distance from the pellet to the target surface was ignored. Therefore, along a vertical shot direction, four kinds of loading (30, 40, 50, and 60 m/s) were carried out in the study of single-pellet simulation.

First, Fig. 10 represents a diagram to describe the change of energy in the single pellet simulation at a velocity of 30 m/s. After the single pellet touching the surface, the kinetic energy gradually transforms into the internal energy for material deformation, and then forming a crater. From 0 to 0.46 μs, the kinetic energy drops from 0.069 mJ to zero, and the internal energy reaches a maximum value of 0.068 mJ. The elastic recovery of the TC2 alloy pushed the pellet off the surface, as the performance of the conversion from material internal energy to pellet kinetic energy. Internal energy remained in the TC2 alloy still near 0.023 mJ after the collision, which leads to plastic deformation and residual stress.

In addition, although the C3D8R unit used in the model meshing improved the calculation efficiency, it also caused an hourglass numerical problem. The artificial strain energy was explained by the hourglass deformation in simulation and the value was only about 2% of the internal energy, which shows little effect on the calculation results.

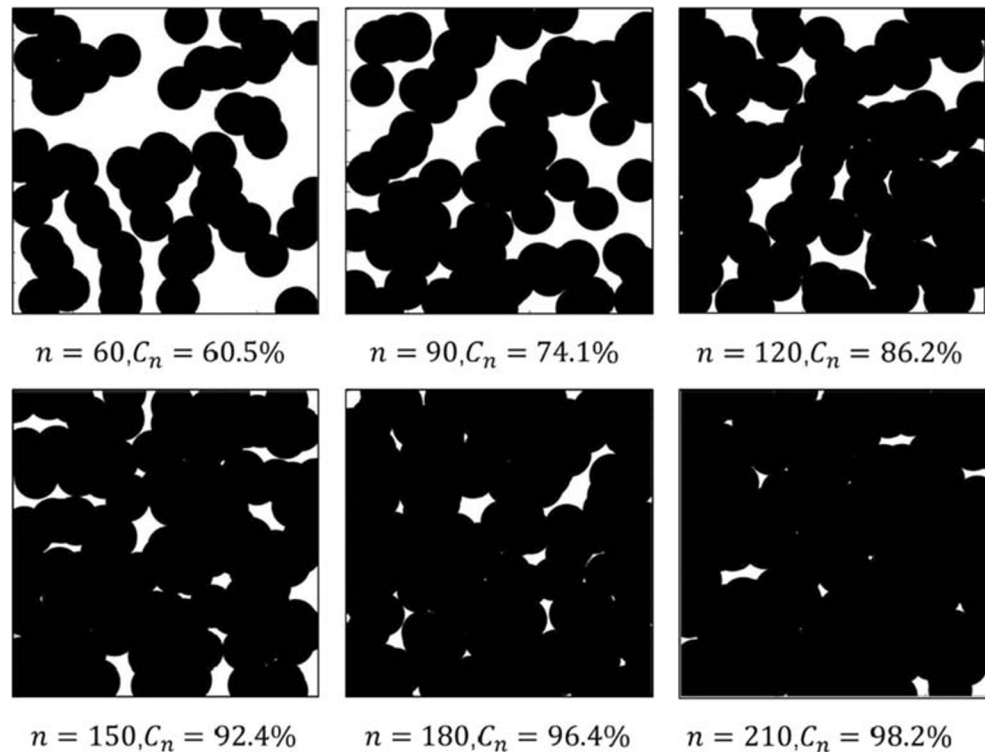
Second, according to the shot peening stress strengthening mechanism, the formation and propagation of the surface crack inhibited mainly due to the transverse residual stress [43]. Therefore, the residual stress studied in this research is the residual stress S_{11} that parallels to the target surface in the numerical simulation. Figure 11a shows the residual stress distribution cloud of the target after a single pellet impact, and Fig. 11b illustrates the changes in residual stress along the depth at different shot peening velocities.

The above-mentioned figures illustrate the fact that a crater appears after a single pellet impact and a residual stress field near the crater. When the pellet rebounded, the elastic recovery of the material acted on the plastically deformed crater and residual compressive stress was generated, while the internal is in a state of tensile stress to achieve equilibrium. As the

Table 2 The crater depth and diameter at different shot peening velocities

Shot peening velocity (m s ⁻¹)	30	40	50	60
Crater depth (μm)	5.87	7.88	9.93	11.63
Crater diameter (μm)	107.6	126.9	143.6	150.9

Fig. 13 The coverage of sprayed zone with n random pellets



depth from the surface increases, the residual compressive stress increases to the maximum and then decreases to zero and even turn to tensile stress. With the impact velocity increased from 30 to 60 m/s, the depth of residual stress increased from 40 to 55 μm , and the maximum residual compressive stress value raised from 1360 to 1570 MPa, while the surface residual compressive stress reduced from 151 to 20 MPa. Therefore, the proper shot peening speed can ensure a good residual stress state, which contains a higher residual compressive stress and a better surface residual compressive stress.

Finally, as shown in Fig. 12, the node displacement along the surface in the crater section was obtained and the displacement curves were plotted under different shot peening velocities. The distance between the two points which are close to the impact center and having zero displacement was taken as the crater diameter. It can be seen clearly that the maximum displacement in the crater section is at the center of the impact crater, and the convexity of the crater edge was deformed by the plastic flow of the TC2 alloy. The higher the shot peening

velocity, the deeper the crater, the larger the crater diameter, and the higher the raised edge. After the measurements, the results of the crater depth and diameter at different velocities are summarized in Table 2.

3.3.2 Determine the value n and shot peening intensity

With the crater diameters at different shot peening velocities and the number of random pellets n , the coverage of the sprayed zone was calculated. In the sprayed zone, the coverage rate C_n is the percentage of crater coverage area, and that is 1 minus the percentage of the non-crater area. First, draw a $1 \times 1 \text{ mm}^2$ rectangle to represent the sprayed area, and then painted craters with projected coordinates from the pellets along the shot peening direction, and finally formed the diagram of coverage at different processes.

Figure 13 illustrates six examples of the coverage of sprayed zone with n random pellets at 50 m/s. When n reaches 90, because of the increasing crater overlap rate, the coverage rate grows slowly as the number of pellets increases. In order

Table 3 Shot peening intensity and n for full coverage at different shot peening velocities

Shot peening velocity (m/s)	Shot peening intensity (mmA)	Number of pellets
30	0.138	460
40	0.170	335
50	0.193	210
60	0.220	160

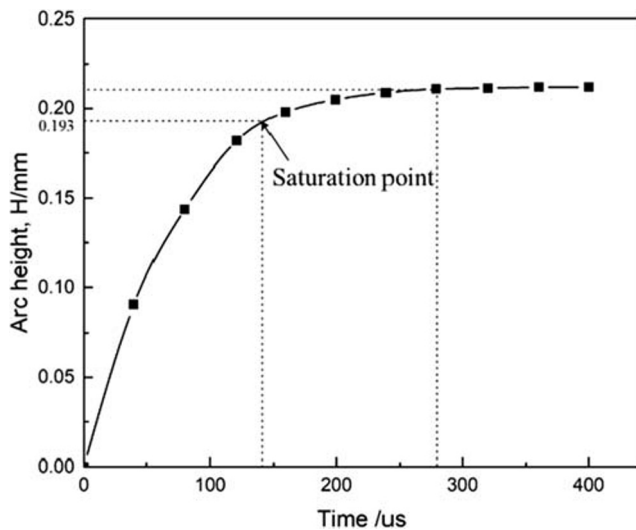
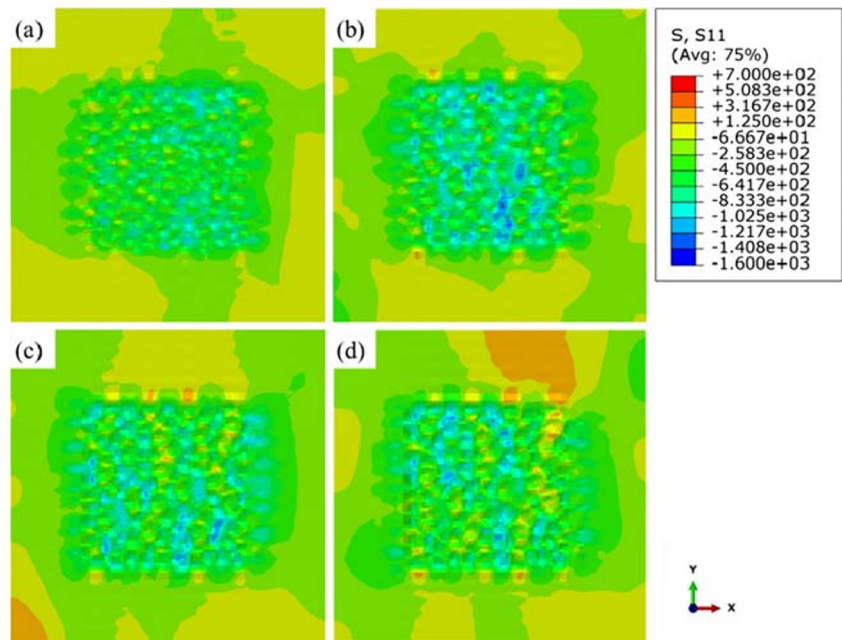


Fig. 14 Calculation curve of arc height in Almen test simulation

to reduce the amount of calculation and ensure the validity of the simulation results, it is considered that a full coverage of shot peening surface was achieved when C_n is greater than 98%.

According to the method described in Section 2.2, a numerical model with n pellets was built to achieve full coverage. Through the standard of SAE J443, the shot peening intensity is the arc height value of a point. As shown in Fig. 14, this point coordinate meets the following condition: when the shot peening time doubled, the exact 10% increments of the arc height were obtained. After simulation and calculation, Table 3 summarizes the shot peening intensity and n for full coverage at different shot peening velocities.

Fig. 15 The surface stress state at different shot peening velocities (a, 30 m/s; b, 40 m/s; c, 50 m/s; d, 60 m/s)



3.3.3 Multiple pellets

At the various shot peening velocities, the residual stress distributions of the TC2 alloy were exhibited with the impact energy. The cloud of residual stress on the surface and along the depth section at different shot peening velocities is illustrated in Fig. 15. It can be seen that when the shot peening velocity increases from 30 to 50 m/s, the surface residual stress and the coverage area both gradually increased. Nevertheless, the two indicators less changed when the velocity reaches 60 m/s, and tensile stress appeared in the sprayed zone because of stress relaxation.

Figure 16 shows the distribution of the residual stress along the depth direction at each velocity. With the increasing shot peening velocity, the compressive residual stress layer becomes deeper and the growing tensile stress area shifts inward gradually. In these cloud pictures, the residual stress ranges from 1700 MPa of compression to 500 MPa of tensile stress. However, the depth of compressive residual stress no longer increases at the velocity 60 m/s, but the area of tensile stress is still expanding.

In order to study the influence of shot peening velocity on the residual stress distribution of the TC2 alloy, the average residual stress at different depths in the study area was calculated with the method mentioned in Section 2.1. The average S_{11} of five nodes at each depth in the simulation result was computed in order along the z direction, and Fig. 17 illustrated the change curves of the average residual stress along the depth direction at different shot peening velocities. The residual compressive stress increases with depth at first, and then decreases to 0 and change into residual tensile stress, and

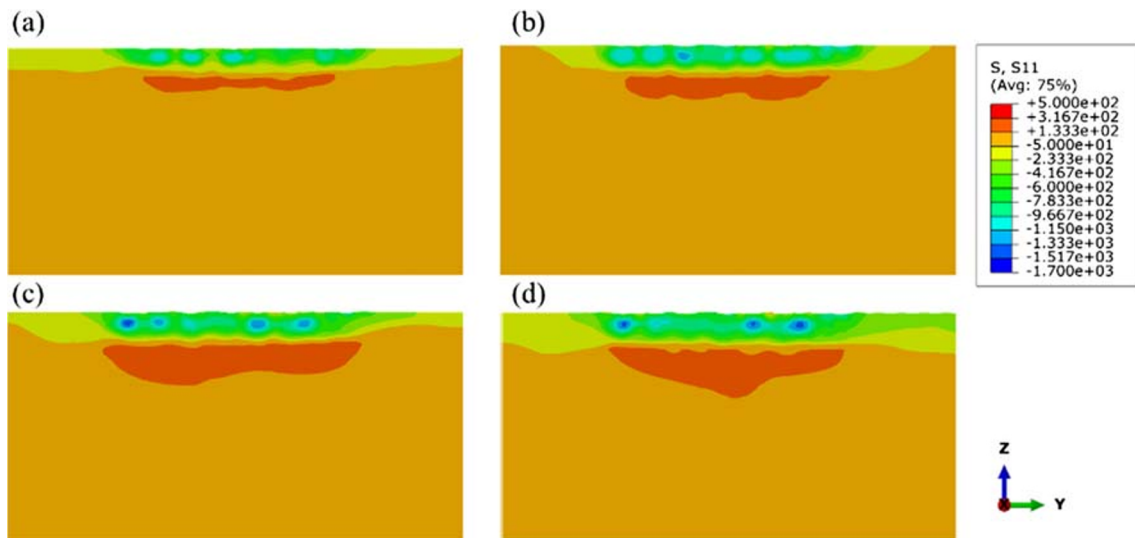


Fig. 16 The distribution cloud of residual stress along the depth section at different shot peening velocities (a, 30 m/s; b, 40 m/s; c, 50 m/s; d, 60 m/s)

finally turn to 0 again at about 0.30 mm depth. Meanwhile, after multiple pellets impact, the maximum residual compressive stress layer becomes deeper, but its value becomes smaller because of the hedging effect, which can be interpreted that the later crater changed the beside crater stress state formed earlier.

3.4 Result in the shot peening test

The shot peening test was carried out with a CNC machine MP4000 according to the experimental procedure mentioned previously, and the material in the test is the as-received TC2 alloy sheet. With the Almen test, the process parameters in the test and simulation were unified by shot peening intensity and coverage. The intensity was determined by pellet diameter, shot gas pressure, and shot peening flow rate, as the calculated intensity at different velocities in Table 3, defined in

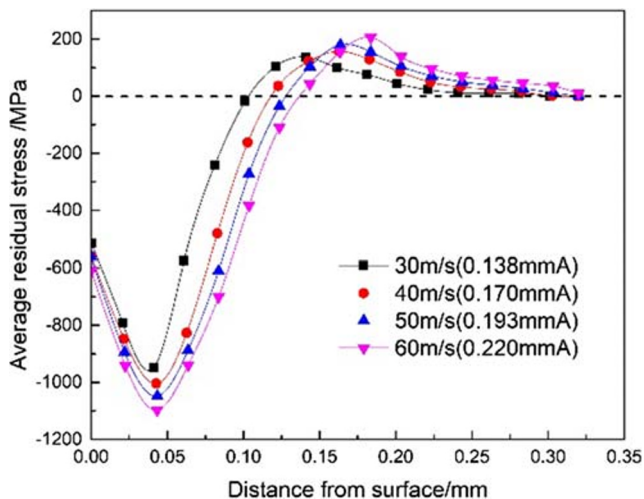


Fig. 17 Distribution curve of the average residual stress along the depth direction at different shot peening velocities

Section 3.3. The consistency in the test and simulation was expressed by the arc height of Almen gage at different conditions. Meanwhile, the processing time was unified with the coverage of at least 98%. The method in the simulation was presented in Section 3.3. While in the shot peening test, the processing time is the time for reaching the coverage. The coverage was expressed by the percentage of blue paint that disappeared in the sprayed zone, which was coated before shot peening.

After shot peening tests, with an X-ray stress tester and portable electrolytic polishing devices, the change curve of the average residual stress along the depth direction at different shot peening intensities was illustrated in Fig. 18.

It can be seen from Fig. 18 that the residual stress distribution after shot peening is consistent with the numerical analysis results. In order to analyze the results of experimental and numerical simulation quantitatively, five eigenvalues were

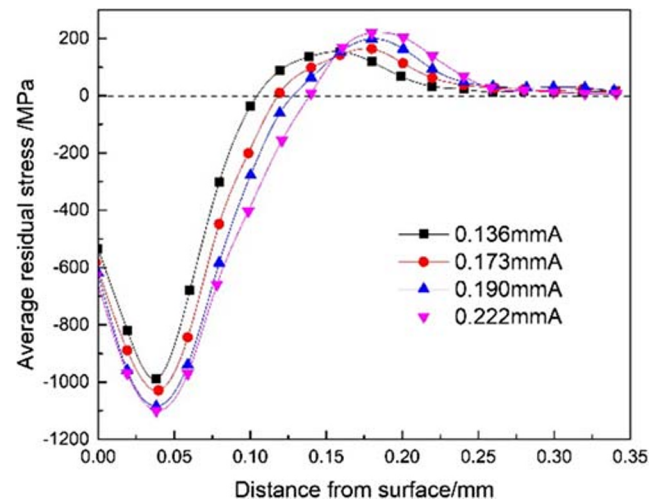


Fig. 18 The average residual stress distribution curve of TC2 alloy with depth after shot peening processes

Table 4 Comparison of residual stress in simulation and test under different shot peening intensities

	Shot peening intensity (mmA)	Surface residual stress (MPa)	Maximum compressive residual stress (MPa)	Depth of maximum compressive stress (um)	Depth of compressive residual stress layer (um)	Maximum tensile residual stress (MPa)
Test	0.136	− 533.5	− 988.4	38.2	103.5	153.7
Simulation	0.138	− 513.0	− 948.8	41.0	103.6	137.4
Error (%)	− 1.5	3.8	4.0	− 7.3	− 0.1	10.6
Test	0.173	− 583.0	− 1029.1	39.7	116.6	163.8
Simulation	0.170	− 559.9	− 1004.5	42.8	118.2	156.5
Error (%)	1.7	4.0	2.4	− 7.8	− 1.4	4.5
Test	0.190	− 618.5	− 1084.3	38.5	128.0	199.2
Simulation	0.193	− 561.9	− 1047.9	43.5	128.3	181.2
Error (%)	− 1.6	9.2	3.4	− 13.0	− 0.2	9.0
Test	0.222	− 629.0	− 1099.5	38.3	139.2	219.3
Simulation	0.220	− 609.1	− 1096.8	43.4	137.8	208.3
Error (%)	0.9	3.2	0.2	− 13.3	1.0	5.0

extracted for comparison at different shot peening intensities, and the comparison results are presented in Table 4. These eigenvalues mainly include surface residual stress, maximum compressive residual stress, depth of maximum compressive stress, depth of compressive residual stress layer and maximum tensile residual stress. Based on the velocity in the simulation, the shot peening tests were carried out at four intensities, i.e., 0.136, 0.173, 0.190, and 0.222 mm A.

As seen from Table 4, the error of the experimental results and the numerical analysis results is not more than 15%, which has a good match. The value of compressive residual stress in the test is higher than that of the simulation, so is the maximum tensile residual stress. The main reasons for these errors analyzed are as follows: First, the interference between the pellets was ignored in the numerical analysis, but there are a lot of pellet collisions in the shot peening test. That is, the number of pellets hitting the target in the shot peening test is significantly more than that of the simulation. Second, the shot peening intensity in the numerical simulation is calculated with formula, while measured in the test, and the error produced [44].

In summary, the material constitutive model at high strain rates and numerical methodology in this study can achieve the prediction of residual stress distribution in the shot peening process, and the simulation results are in good agreement with the experimental results.

4 Conclusions

1. During the high strain rate deformation, the TC2 alloy exhibits an obvious effect of strain rate plasticizing and enhancement, and the dispersed β particles are the

important reasons that the width of ASBs changes insignificantly at different strain rates.

2. The modified Johnson-Cook model with adiabatic temperature rise can better characterize the dynamic rheological behavior of the TC2 alloy, a good prediction accuracy expressed by the AARE = 0.9949 and the R = 1.04%.
3. Based on the scientific construction of the simulation model and the rationalization of process parameters, this simulation can better predict the residual stress distribution of TC2 alloy during the actual process.

Acknowledgments The authors gratefully acknowledge the support from the Aeronautical Science Foundation of China (20153021001).

References

1. Jiang ZD (2013) Study on microstructure and properties of CO₂ laser welding butt weld joints of TC2 titanium alloy sheets. *Electric Welding Machine* 43:80–82. <https://doi.org/10.7512/j.issn.1001-2303.2013.08.19>
2. Zong YY, Shao B, Wang XG, Guo B, Shan DB. (2018) Effect of hydrogen on phase transformation, thermal deformation behavior, and forming limit of TC2 alloy. *Adv Eng Mater*, 20. <https://doi.org/10.1002/adem.201800690>
3. Li Y, Pei Z, Zaman B, Zhang Y, Yuan H, Cao B. (2018) Effects of plastic deformations on the electrochemical and stress corrosion cracking behaviors of TC2 titanium alloy in simulated seawater. *Materials Research Express*, 5. <https://doi.org/10.1088/2053-1591/aadc44>
4. Harrison J (1987) Controlled shot peening: cold working to improve fatigue strength. *Heat Treat* 19:16–18
5. Ghorashi MS, Farrahi GH, Movahhedy MR (2019) Effect of severe shot peening on the fatigue life of the laser-cladded Inconel 718 specimens. *Int J Adv Manuf Technol* 104(5–8):2619–2631. <https://doi.org/10.1007/s00170-019-04082-6>
6. Torres M, Voorwald H (2002) An evaluation of shot peening, residual stress and stress relaxation on the fatigue life of AISI 4340

- steel. *Int J Fatigue* 24:877–886. [https://doi.org/10.1016/S0142-1123\(01\)00205-5](https://doi.org/10.1016/S0142-1123(01)00205-5)
7. Meguid SA (1991) Effect of partial-coverage upon the fatigue fracture behaviour of peened components. *Fatigue Fract Eng Mater Struct* 14:515–530. <https://doi.org/10.1111/j.1460-2695.1991.tb00680.x>
 8. Zimmermann M, Klemenz M, Schulze V (2010) Literature review on shot peening simulation. *Int J Comput Mater Sci Surf Eng* 3:289. <https://doi.org/10.1504/IJCMSE.2010.036218>
 9. Silva DP, Bastos IN, Fonseca MC (2020) Influence of surface quality on residual stress of API 5L X80 steel submitted to static load and its prediction by artificial neural networks. *Int J Adv Manuf Technol* 108(11–12):3753–3764. <https://doi.org/10.1007/s00170-020-05621-2>
 10. Wang C, Wang C, Wang L, Lai Y, Li K, Zhou Y (2020) A dislocation density-based comparative study of grain refinement, residual stresses, and surface roughness induced by shot peening and surface mechanical attrition treatment. *Int J Adv Manuf Technol* 108(1–2):505–525. <https://doi.org/10.1007/s00170-020-05413-8>
 11. Elmagd E, Abouridouane M (2006) Characterization, modelling and simulation of deformation and fracture behaviour of the light-weight wrought alloys under high strain rate loading. *Int J Impact Eng* 32:741–758. <https://doi.org/10.1016/j.ijimpeng.2005.03.008>
 12. Ali T, Wang L, Cheng X, Liu A, Xu X (2019) Omega phase formation and deformation mechanism in heat treated Ti-5553 alloy under high strain rate compression. *Mater Lett* 236:163–166. <https://doi.org/10.1016/j.matlet.2018.10.057>
 13. Yi XB, Zhang JX, Li BD, Guo XR, Li XF, Chang WC. (2019) Dynamic compressive mechanical properties of TB6 titanium alloy under high temperature and high strain rate. *Rare Metal Materials and Engineering*, 48:1220–1224. WOS: 000467321400030
 14. Skubisz P, Lisiecki L, Packo M, Skowronek T, Micek P, Tokarski T. (2018) Effect of high strain rate beta processing on microstructure and mechanical properties of near- titanium alloy Ti-10V-2Fe-3Al. *Proceedings of the Institution of Mechanical Engineers Part L—Journal of Materials-Design and Applications*, 232:181–190. <https://doi.org/10.1177/1464420715619447>
 15. Brozek C, Sun F, Vermaut P, Millet Y, Lenain A, Embury D, Jacques PJ, Prima F (2016) A beta-titanium alloy with extra high strain-hardening rate: design and mechanical properties. *Scr Mater* 114:60–64. <https://doi.org/10.1016/j.scriptamat.2015.11.020>
 16. Huang GQ, Xie LS, Chen MH, Si SS, Wu RH (2019) Flow stress characteristics and constitutive relation of Ti2AlNb alloy under high strain rate. *Rare Metal Mater Eng* 48:847–852 WOS: 000463845300023
 17. Zheng Y, Zeng W, Wang Y, Zhou D, Gao X (2017) High strain rate compression behavior of a heavily stabilized beta titanium alloy: kink deformation and adiabatic shearing. *J Alloys Compd* 708:84–92. <https://doi.org/10.1016/j.jallcom.2017.02.284>
 18. Steinberg DJ, Cochran SG, Guinan MW (1980) A constitutive model for metals applicable at high-strain rate. *J Appl Phys* 51: 1498–1504. <https://doi.org/10.1063/1.327799>
 19. Zerilli FJ, Armstrong RW (1987) Dislocation-mechanics-based constitutive relations for material dynamics calculations. *J Appl Phys* 61:1816–1825. <https://doi.org/10.1063/1.338024>
 20. Cook GRJA (1985) Fracture characteristics of three metals subjected to various strains, strain rates, temperatures and pressures. *Eng Fract Mech*. [https://doi.org/10.1016/0013-7944\(85\)90052-9](https://doi.org/10.1016/0013-7944(85)90052-9)
 21. Bhalerao, Nitin B, Joshi, Suhas S, Naik et al (2018) High strain rate and high temperature behavior of Ti-6Al-4V alloy under compressive loading. *J Eng Mater Technol* 140. <https://doi.org/10.1115/1.4038671>
 22. Che JT, Zhou TF, Liang ZQ, Wu JJ, Wang XB (2018) An integrated Johnson-Cook and Zerilli-Armstrong model for material flow behavior of Ti-6Al-4V at high strain rate and elevated temperature. *J Braz Soc Mech Sci Eng* 40. <https://doi.org/10.1007/s40430-018-1168-7>
 23. Ara B, Ramin G, Mario G (2012) On the shot peening surface coverage and its assessment by means of finite element simulation: a critical review and some original development. *Appl Surf Sci* 259: 186–194. <https://doi.org/10.1016/j.apsusc.2012.07.017>
 24. Mohamed J, Augustin G, Julie L, Oussama et al (2016) Robust methodology to simulate real shot peening process using discrete-continuum coupling method. *Int J Mech Sci* 107:21–33. <https://doi.org/10.1016/j.ijmecsci.2016.01.005>
 25. Kim T, Lee H, Kim M, Jung S (2012) A 3D FE model for evaluation of peening residual stress under angled multi-shot impacts. *Surf Coat Technol* 206:3981–3988. <https://doi.org/10.1016/j.surfcoat.2012.03.078>
 26. Dassault Systèmes. Abaqus 6.12 online documentation. Providence, RI: Dassault Systèmes, 2012
 27. Chen JS, Desai DA, Heyns SP, Pietra F (2019) Literature review of numerical simulation and optimisation of the shot peening process. *Advances in. Mech Eng* 11(3):168781401881827. <https://doi.org/10.1177/1687814018818277>
 28. Elbella A, Rami V, Hogirala J. A sensitivity analysis of shot peening parameters. In: ASME 2006 International design engineering technical conferences & computers and information in engineering conference (IDETC/CIE), Philadelphia, PA, 10–13 September 2006. New York: ASME
 29. Kim T, Jin HL, Lee H, Cheong SK (2010) An area-average approach to peening residual stress under multi-impacts using a three-dimensional symmetry-cell finite element model with plastic shots. *Mater Des* 31:50–59. <https://doi.org/10.1016/j.matdes.2009.07.032>
 30. Farrahi GH, Lebrijn JL, Couratin D (2007) Effect of shot peening on residual stress and fatigue life of a spring steel. *Fatigue Fract Eng Mater Struct* 18:211–220. <https://doi.org/10.1111/j.1460-2695.1995.tb00156.x>
 31. Curtis S, Rios ERDL, Rodopoulos CA, Levers A (2003) Analysis of the effects of controlled shot peening on fatigue damage of high strength aluminium alloys. *Int J Fatigue* 25:59–66. [https://doi.org/10.1016/S0142-1123\(02\)00049-X](https://doi.org/10.1016/S0142-1123(02)00049-X)
 32. Tekeli S (2002) Enhancement of fatigue strength of SAE 9245 steel by shot peening. *Mater Lett* 57:604–608. [https://doi.org/10.1016/S0167-577X\(02\)00838-8](https://doi.org/10.1016/S0167-577X(02)00838-8)
 33. Xiao X, Sun Y, Zhao R, Yang M, Gao G, Li Y (2019) A design for lumped mass of a shot model in random peening simulation and prediction of dimple size evolution. *Int J Adv Manuf Technol* 103(9–12):4597–4608. <https://doi.org/10.1007/s00170-019-03581-w>
 34. Xiang J, Pang S, Xie L, Cheng G, Liang R, Gao F, Bai L (2018) A numerically low-cost and high-accuracy periodic FE modeling of shot-peened 34CrNiMo6 and experimental validation. *Int J Adv Manuf Technol* 97(5–8):1673–1685. <https://doi.org/10.1007/s00170-018-2029-3>
 35. Gangaraj SMH, Guagliano M, Farrahi GH (2014) An approach to relate shot peening finite element simulation to the actual coverage. *Surf Coat Technol* 243:39–45. <https://doi.org/10.1016/j.surfcoat.2012.03.057>
 36. Miao HY, Larose S, Perron C, Levesque M (2009) On the potential applications of a 3D random finite element model for the simulation of shot peening. *Adv Eng Softw* 40:1023–1038. <https://doi.org/10.1016/j.advengsoft.2009.03.013>
 37. Majzoubi GH, Azizi R, Nia AA. (2005) A three-dimensional simulation of shot peening process using multiple shot impacts. *Journal of Materials Processing Technology*, 164–165:1226–1234. doi: <https://doi.org/10.1016/j.jmatprotec.2005.02.139>

38. Stranart SAMA (2002) 3D FE analysis of peening of strain-rate sensitive materials using multiple impingement model. *Int J Impact Eng* 27:119–134. [https://doi.org/10.1016/s0734-743x\(01\)00043-4](https://doi.org/10.1016/s0734-743x(01)00043-4)
39. Zhuo C, Fan Y, Meguid SA (2014) Realistic finite element simulations of arc-height development in shot-peened Almen strips. *J Eng Mater Technol* 136:41001–41002. <https://doi.org/10.1115/1.4028006>
40. Huang XF, Liu ZW, Xie HM (2013) Recent progress in residual stress measurement techniques. *Acta Mechanica Solida Sinica* 26: 570–583 CNKI:SUN:GTLB.0.2013-06-002
41. Kim T, Lee H, Jung S, Jin HL (2012) A 3D FE model with plastic shot for evaluation of equi-biaxial peening residual stress due to multi-impacts. *Surf Coat Technol* 206:3125–3136. <https://doi.org/10.1016/j.surfcoat.2011.12.042>
42. Teo A, Ahluwalia K, Aramcharoen A (2020) Experimental investigation of shot peening: correlation of pressure and shot velocity to Almen intensity. *Int J Adv Manuf Technol* 106(11):4859–4868. <https://doi.org/10.1007/s00170-020-04982-y>
43. Li Y (2011) Shot stream finite element model for shot peening numerical simulation and its experiment study. *J Mech Eng* 47: 43. <https://doi.org/10.3901/JME.2011.22.043>
44. Hu DY, Gao Y, Meng FC, Song J, Wang YF, Ren MX, Wang RQ (2017) A unifying approach in simulating the shot peening process using a 3D random representative volume finite element model. *Chin J Aeronaut* 030:1592–1602. <https://doi.org/10.1016/j.cja.2016.11.005>

Publisher's note Springer Nature remains neutral with regard to jurisdictional claims in published maps and institutional affiliations.